HAL
open science

VVDS-SWIRE. Clustering evolution from a spectroscopic sample of galaxies with redshift 0.2 < z < 2.1 selected from Spitzer IRAC 3.6 mum and 4.5 mum photometry

Sylvain de la Torre, Olivier Le Fèvre, S. Arnouts, L. Guzzo, D. Farrah, Angela Iovino, C. J. Lonsdale, Baptiste Meneux, Seb Oliver, Agnieszka Pollo, et al.

To cite this version:

Sylvain de la Torre, Olivier Le Fèvre, S. Arnouts, L. Guzzo, D. Farrah, et al.. VVDS-SWIRE. Clustering evolution from a spectroscopic sample of galaxies with redshift 0.2 < z < 2.1 selected from Spitzer IRAC 3.6 mum and 4.5 mum photometry. Astronomy and Astrophysics - A&A, 2007, 475, pp.443-451. 10.1051/0004-6361:20077161 . hal-03733007

HAL Id: hal-03733007

https://hal.science/hal-03733007v1

Submitted on 17 Sep 2022

HAL is a multi-disciplinary open access archive for the deposit and dissemination of scientific research documents, whether they are published or not. The documents may come from teaching and research institutions in France or abroad, or from public or private research centers.

L'archive ouverte pluridisciplinaire **HAL**, est destinée au dépôt et à la diffusion de documents scientifiques de niveau recherche, publiés ou non, émanant des établissements d'enseignement et de recherche français ou étrangers, des laboratoires publics ou privés.

A&A 475, 443–451 (2007)
DOI: 10.1051/0004-6361:20077161
© ESO 2007

Astronomy & Astrophysics

VVDS-SWIRE*

Clustering evolution from a spectroscopic sample of galaxies with redshift 0.2 < z < 2.1 selected from Spitzer IRAC 3.6 μm and 4.5 μm photometry

S. de la Torre[1], O. Le Fèvre[1], S. Arnouts[1], L. Guzzo[2], D. Farrah[3], A. Iovino[2], C. J. Lonsdale[4,5], B. Meneux[2,6], S. J. Oliver[7], A. Pollo[1,21], I. Waddington[7], D. Bottini[6], F. Fang[10], B. Garilli[6], V. Le Brun[1], D. Maccagni[6], J. P. Picat[13], R. Scaramella[9,18], M. Scodeggio[6], D. Shupe[4], J. Surace[10], L. Tresse[1], G. Vettolani[9], A. Zanichelli[9], C. Adami[1], S. Bardelli[8], M. Bolzonella[8], A. Cappi[8], S. Charlot[14,15], P. Ciliegi[8], T. Contini[13], S. Foucaud[26], P. Franzetti[6], I. Gavignaud[17], O. Ilbert[25], F. Lamareille[12], H. J. McCracken[15,16], B. Marano[12], C. Marinoni[23], A. Mazure[1], R. Merighi[8], S. Paltani[20,21], R. Pellò[13], L. Pozzetti[8], M. Radovich[11], G. Zamorani[8], E. Zucca[8], M. Bondi[9], A. Bongiorno[12], J. Brinchmann[24], O. Cucciati[2,19], Y. Mellier[15,16], P. Merluzzi[11], S. Temporin[2], D. Vergani[6], and C. J. Walcher[1]

(Affiliations can be found after the references)

Received 24 January 2007 / Accepted 26 July 2007

ABSTRACT

Aims. By combining data from the VIMOS VLT Deep Survey (VVDS) with the Spitzer Wide-area InfraRed Extragalactic survey (SWIRE), we have built the currently largest spectroscopic sample of high redshift galaxies selected in the rest-frame near-infrared. We have obtained 2040 spectroscopic redshifts of galaxies with $(m_{3.6})_{\rm AB} < 21.5$ at 3.6 μm, and 1255 spectroscopic redshifts of galaxies with $(m_{4.5})_{\rm AB} < 21$. These allow us to investigate the clustering evolution of galaxies selected via their rest-frame near-infrared luminosity in the redshift range $0.2 < z < 2.1$.

Methods. We use the projected two-point correlation function $w_{\rm p}(r_{\rm p})$ to study the three dimensional clustering properties of galaxies detected at 3.6 μm and 4.5 μm with the InfraRed Array Camera (IRAC) in the SWIRE survey with measured spectroscopic redshifts from the first epoch VVDS. We compare these properties to those of a larger sample of 16672 SWIRE galaxies for which we have accurate photometric redshifts in the same field.

Results. We find that in the 3.6 μm and 4.5 μm flux limited samples, the apparent correlation length does not change from redshift ~2 to the present. The measured correlation lengths have a mean value of $r_0 \simeq 3.9 \pm 0.5\ h^{-1}$ Mpc for the galaxies selected at 3.6 μm and a mean value of $r_0 \simeq 4.4 \pm 0.5\ h^{-1}$ Mpc for the galaxies selected at 4.5 μm, across the whole redshift range explored. These values are larger than those typicaly found for I-band selected galaxies at $I_{\rm AB} < 24$, for which r_0 varies from 2.69 h^{-1} Mpc to 3.63 h^{-1} Mpc between $z = 0.5$ to $z = 2.1$. We find that the difference in correlation length between I-band and 3.6–4.5 μm selected samples decreases with increasing redshift, becoming comparable at $z \simeq 1.5$. We interpret this as evidence that galaxies with older stellar populations and galaxies actively forming stars reside in comparably over-dense environments at epochs earlier than $z \simeq 1.5$, supporting the recently reported flattening of the color-density relation at high redshift. The increasing difference in correlation length with cosmic time observed between rest-frame UV-optical and near-infrared selected samples could then be an indication that star formation is gradually shifting to lower density regions with decreasing redshift, while the older, passively evolving galaxies remain in the most over-dense peaks.

Key words. cosmology: observations – cosmology: large-scale structure of Universe – galaxies: evolution – galaxies: high-redshift – galaxies: statistics – infrared: galaxies

1. Introduction

According to the current cosmological paradigm, the formation of large scale structures can be described as the evolution of primordial dark matter mass density perturbations under the influence of gravity. The galaxies that we observe are the result of the cooling and fragmentation of gas within the potential wells provided by the dark matter halos, which build up hierarchically (White & Rees 1978). Even if the distribution of galaxies is in some way biased with respect to the distribution of the dark matter (Kaiser 1984), the spatial distribution of galaxies should therefore trace the dark matter density field.

It is to be expected that the physical processes that build galaxies of different types and luminosities are sensitive to the mass of halos and their different environments. Therefore, the evolution of the clustering of galaxies may depend on galaxy type, luminosity and environment. A comparison of the clustering of different galaxy populations with redshift could therefore provide useful constraints on the evolution and formation scenario of galaxies.

* Based on data obtained with the European Southern Observatory Very Large Telescope, Paranal, Chile, program 070.A-9007(A), and on data obtained at the Canada-France-Hawaii Telescope, operated by the CNRS of France, CNRC in Canada and the University of Hawaii, and observations obtained with MegaPrime/MegaCam, a joint project of CFHT and CEA/DAPNIA, at the Canada-France-Hawaii Telescope (CFHT) which is operated by the National Research Council (NRC) of Canada, the Institut National des Science de l'Univers of the Centre National de la Recherche Scientifique (CNRS) of France, and the University of Hawaii. This work is based in part on data products produced at TERAPIX and the Canadian Astronomy Data Centre as part of the Canada-France-Hawaii Telescope Legacy Survey, a collaborative project of NRC and CNRS.

Article published by EDP Sciences and available at http://www.aanda.org or http://dx.doi.org/10.1051/0004-6361:20077161

Observations of galaxies at redder wavelengths, up to a few microns rest-frame, preferentially selects older stellar populations formed earlier in the history of the Universe. As older stars are likely to have formed in higher density peaks in the underlying mass distribution, it is therefore expected that the clustering of their host galaxies will be significantly higher than that of galaxies hosting more recently formed stars. This expectation already has some observational evidence; for example, in the local Universe, selecting galaxies at 2.15 μm (K_s band) from the Two Micron All Sky Survey (2MASS, Maller et al. 2005), it is found that these galaxies are more clustered than those selected at optical wavelengths, with an angular correlation amplitude several times larger than found in the Sloan Digital Sky Survey Early Data Release (SDSS EDR, Connolly et al. 2002). At higher redshifts, Oliver et al. (2004), using Spitzer data, found that at $z_{\rm median} \simeq 0.75$ the correlation length of $(m_{3.6})_{\rm AB} < 20.1$ (or equivalently $K_{\rm Vega} < 18.7$) selected galaxies is $r_0 = 4.4 \pm 0.1\ h^{-1}$ Mpc with an angular correlation amplitude ~60 times lower than for 2MASS local galaxies, and recent work has shown that more infrared-luminous galaxies are even more strongly clustered (Farrah et al. 2006).

The IRAC 3.6 μm and 4.5 μm bands are only marginally affected by the first polycyclic aromatic hydrocarbon (PAH) spectral feature at 3.3 μm, which fall in these bands in the redshift ranges [0, 0.18] and [0.21, 0.51] respectively. However, galaxy populations observed in these bands contain a mix of early-type, dust-reddened, and star-forming systems (Rowan-Robinson et al. 2005) which make clustering expectations non-trivial.

This paper aims to characterize the evolution of the real-space correlation length r_0 of near-infrared selected galaxies from the Spitzer Wide-area InfraRed Extragalactic survey (SWIRE, Lonsdale et al. 2003), which have secure spectroscopic redshifts from the VIMOS VLT Deep Survey (VVDS, Le Fèvre et al. 2005b). We compare these measurements to those in shallower samples, e.g. Oliver et al. (2004), as well as to the observed evolution of optically-selected galaxies as shown in Le Fèvre et al. (2005a), up to $z \simeq 2$.

In Sect. 2 we describe the galaxy sample that we use for this analysis. We present in Sect. 3 the formalism of the two-point correlation function and the results. Finally in Sect. 4 we discuss the observed clustering evolution and our conclusions.

Throughout this analysis we assume a flat ΛCDM cosmology with $\Omega_M = 0.3$, $\Omega_\Lambda = 0.7$, $\sigma_8 = 0.9$ and $H_0 = 100\ h$ km s^{-1} Mpc^{-1}, while a value of $H_0 = 70$ km s^{-1} Mpc^{-1} is used when computing absolute magnitudes.

2. The VVDS-SWIRE sample

The VVDS-SWIRE field is the intersection of the VIRMOS Deep Imaging Survey (VDIS, Le Fèvre et al. 2004) and the SWIRE-XMM/LSS fields. The total area covered on the sky is ~0.82 deg^2. From this field we extract two galaxy samples. The larger one consists of those SWIRE galaxies for which we measured photometric redshifts, hereafter referred to as the *photometric redshift sample*. The technique that we use to measure photometric redshifts is presented in the next section. The other sample, hereafter the *spectroscopic redshift sample*, contains galaxies included in a sub-area of ~0.42 deg^2, which corresponds to a fraction of the VVDS-Deep survey (Le Fèvre et al. 2005b) area and for which we have spectroscopic redshifts measured during the VVDS first epoch observations. We restrict this sample to galaxies with secure redshifts, i.e. with a redshift confidence level greater than 80% (flag 2 to 9, Le Fèvre et al. 2005b). About 25% of the galaxy population is randomly sampled and we are correcting the correlation measurements for geometrical effects, e.g. on small scales, as described in Sect. 3 and in Pollo et al. (2005). In these two samples the star-galaxy separation has been performed first by using optical and mid-infrared colors to define the locus of Galactic stars. In addition, we used the spectral energy distribution (SED) template fitting procedure to reject any remaining stars and QSO. Objects which are best fitted with a star or a QSO SED template and which have a high SExtractor (Bertin & Arnouts 1996) stellarity index in the i' band (CLASS_STAR > 0.97) have been removed from the samples. The full description of the data-set and its properties is given in Le Fèvre et al. (2007, in preparation).

2.1. Photometric redshifts

The photometric redshifts have been estimated using the χ^2 fitting algorithm *Le Phare*[1] and calibrated with the VVDS first epoch spectroscopic redshifts in the same data-set as described in Ilbert et al. (2006), including in addition the 3.6 μm and 4.5 μm infrared photometry from SWIRE (Lonsdale et al. 2003). The photometric data cover the wavelength domain 0.3 μm $\leq \lambda \leq$ 5.0 μm, including B, V, R, I from VDIS (Le Fèvre et al. 2004), u^*, g', r', i', z' from the Canada France Hawaii Telescope Legacy Survey (CFHTLS-D1, McCracken et al., in preparation), K-band from VDIS (Iovino et al. 2005) and the 3.6 μm and 4.5 μm infrared photometry from SWIRE (Lonsdale et al. 2003). The empirical templates used by Ilbert et al. (2006) have been extended to the mid-infrared domain using the GISSEL library (Bruzual & Charlot 2003). We use the spectroscopic sample to simultaneously adapt the templates and the zero-point calibrations (Ilbert et al. 2006). The comparison with 1500 spectroscopic redshifts from the VVDS first epoch data shows an accuracy of $\sigma_{\Delta z/(1+z)} \simeq 0.031$ with a small fraction of catastrophic errors; 1.7% objects with $|\Delta z| > 0.15(1+z)$, up to a redshift $z \sim 2$. A full description of the method and the data used to compute these photometric redshifts is given in Ilbert et al. (2006) and Arnouts et al. (2007, in preparation).

2.2. Selection functions

We split the spectroscopic redshift and photometric redshift samples into two sub-samples, applying a simple magnitude selection from observed fluxes on the 3.6 μm and 4.5 μm bands. These sub-samples satisfy respectively a magnitude in the AB system measured in the 3.6 μm band of $(m_{3.6})_{\rm AB} < 21.5$ and in the 4.5 μm band of $(m_{4.5})_{\rm AB} < 21$ or, equivalently $S_{3.6} > 9.2\ \mu$Jy and $S_{4.5} > 14.5\ \mu$Jy. These criteria correspond to the limits of completeness for the SWIRE bands (Le Fèvre et al. 2007, in preparation). In addition, the spectroscopic redshift sample has a $I_{\rm AB}$ cut, as the VVDS-Deep spectroscopic sample is a magnitude-selected sample according to the criterion $17.5 < I_{\rm AB} < 24$.

The $I_{\rm AB}$ cut introduces a color dependent incompleteness in terms of SWIRE magnitudes in the spectroscopic redshift sample. We lose a small fraction of faint and red objects, as shown in Figs. 1 and 2 for the 3.6 μm and 4.5 μm galaxies. We estimate the fraction of lost galaxies to be, respectively, 11.6% and 10.3%. To understand the population missed in the spectroscopic sample we have used the photometric redshifts described in the previous section. We find that the galaxies that we are missing in the 4.5 μm spectroscopic redshift sub-sample are redder than those in the 3.6 μm spectroscopic sub-sample. The median $(I - m_{3.6})_{\rm AB}$ color of these sub-samples are 3.72 and 3.67

[1] http://www.oamp.fr/arnouts/LE_PHARE.html

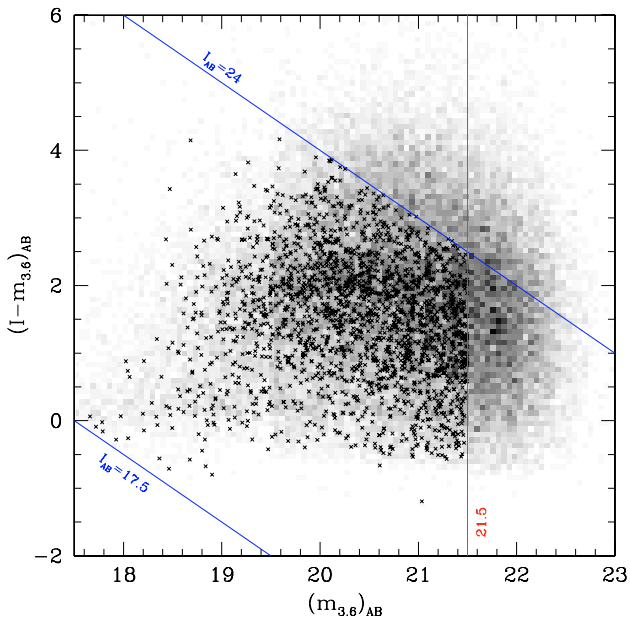

Fig. 1. Color-magnitude diagram for the 3.6 μm spectroscopic and photometric sub-samples. All the galaxies detected at 3.6 μm in the VVDS-SWIRE field are shown in grey scale. The photometric redshift sub-sample consists of all the objects with $(m_{3.6})_{AB} < 21.5$. Galaxies from the spectroscopic sub-sample are shown as crosses. The vertical line indicates the limit of completeness, and the two diagonal lines show the limits of the spectroscopic selection; $17.5 < I_{AB} < 24$. We estimate that the fraction of galaxies we lose in the spectroscopic redshift sub-sample due to the VVDS spectroscopic selection, assuming the completeness limit of $(m_{3.6})_{AB} < 21.5$, is 11.6%.

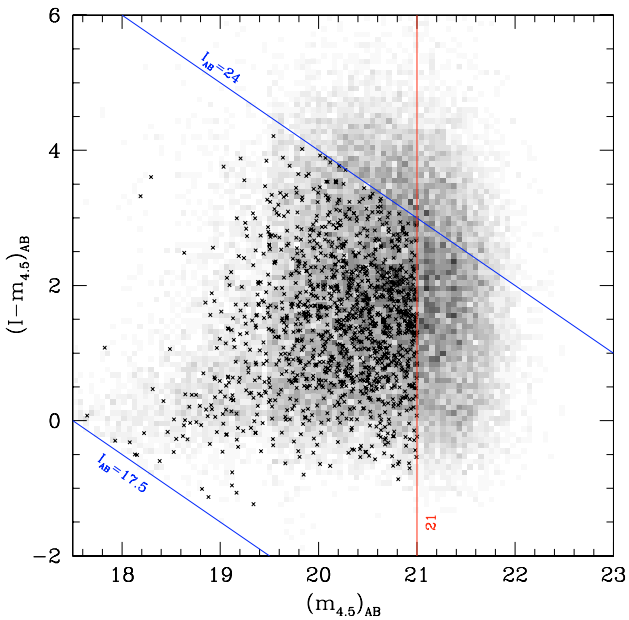

Fig. 2. Color-magnitude diagram for the 4.5 μm spectroscopic and photometric sub-samples. All the galaxies detected at 4.5 μm in the VVDS-SWIRE field are represented in grey scale. The photometric redshift sub-sample consists of all the objects with $(m_{4.5})_{AB} < 21$. Galaxies from the spectroscopic sub-sample are shown as crosses. The vertical line indicates the limit of completeness and the two diagonal lines show the limits of the spectroscopic selection; $17.5 < I_{AB} < 24$. We estimate that the fraction of galaxies we lose in the spectroscopic redshift sub-sample due to the VVDS spectroscopic selection, assuming the completeness limit $(m_{4.5})_{AB} < 21$, is 10.3%.

respectively, as shown in Fig. 3. We note that photometric redshifts may have difficulties in identifying dust obscured AGN because we are lacking the redder bands, e.g. Spitzer-MIPS 24 μm. However, the fraction of dust reddened AGN is expected to be low (Tajer et al. 2007), and its impact on clustering properties should be insignificant. Therefore, the photometric redshift sample, which is assumed to be complete and free of significant contaminants, allows us to evaluate the effect of the color dependent magnitude incompleteness on the clustering measurements performed on the spectroscopic redshift sample.

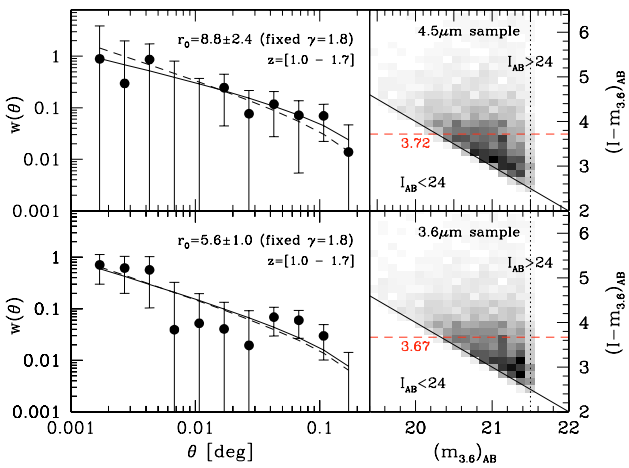

Fig. 3. The *right panels* present the color-magnitude diagrams $(I - m_{3.6})_{AB}$ versus $(m_{3.6})_{AB}$ for the 3.6 μm (*top*) and 4.5 μm (*bottom*) photometric sub-samples, considering the objects that fall above the spectroscopic selection upper limit $I_{AB} = 24$. The galaxy number density is shown in grey scale and the dashed line indicates the median of the $(I - m_{3.6})_{AB}$ distributions. In the left panels are the angular correlation function for these two selections in the redshift range $z_{phot} = [1, 1.7]$. In these panels the solid lines show the best-fit model when letting the two parameters vary, while the dashed lines indicate the best-fit model with fixed $\gamma = 1.8$.

3. Clustering measurements

3.1. Methods

3.1.1. Computing the projected correlation function

The method applied to compute the projected correlation function and to derive the real-space correlation length r_0 and the correlation function slope γ, is described in Pollo et al. (2005). We present in this section the main points of the method.

First we evaluate the bi-dimensional two-point correlation function $\xi(r_p, \pi)$ using the standard Landy and Szalay estimator (Landy & Szalay 1993). This estimator of the two-point correlation function is defined as:

$$\xi(r) = \frac{GG(r) - 2GR(r) + RR(r)}{RR(r)} \quad (1)$$

where $GG(r)$, $RR(r)$ and $GR(r)$ are the normalized numbers of independent galaxy-galaxy, galaxy-random and random-random pairs with comoving separation between r and $r + \mathrm{d}r$.

The three-dimensional galaxy space distribution recovered from a redshift survey and its two-point correlation function $\xi(s)$, are distorted due to the effect of galaxy peculiar velocities. Therefore, the redshift-space separation s differs from the comoving separation r. These distortions occur only radially since

peculiar velocities affect only redshift. Thus we compute the bi-dimensional two-point correlation $\xi(r_\mathrm{p}, \pi)$ by splitting the separation vector s into two components: r_p and π, perpendicular and parallel respectively to the line of sight (Fisher et al. 1994). In this way, we separate the redshift distortions from the true spatial correlations.

Then, we project $\xi(r_\mathrm{p}, \pi)$ along the line of sight, onto the r_p axis. This allows to integrate out the dilution produced by the redshift-space distortion field and we obtain the projected two-point correlation function:

$$w_\mathrm{p}(r_\mathrm{p}) = 2\int_0^\infty \xi(r_\mathrm{p}, \pi)\mathrm{d}\pi = 2\int_0^\infty \xi\left(\sqrt{r_\mathrm{p}^2 + y^2}\right)\mathrm{d}y. \quad (2)$$

In practice, the upper integration limit has to be finite, therefore we choose its optimal value as 20 h^{-1} Mpc (Pollo et al. 2005). Assuming a power-law form for $\xi(r)$, i.e. $\xi(r) = (r_0/r)^\gamma$, one can write $w_\mathrm{p}(r_\mathrm{p})$ as,

$$w_\mathrm{p}(r_\mathrm{p}) = r_\mathrm{p}\left(\frac{r_0}{r_\mathrm{p}}\right)^\gamma \frac{\Gamma\left(\frac{1}{2}\right)\Gamma\left(\frac{\gamma-1}{2}\right)}{\Gamma\left(\frac{\gamma}{2}\right)} \quad (3)$$

where Γ is the Euler Gamma function.

We fit the $w_\mathrm{p}(r_\mathrm{p})$ measurements to a power-law model (Eq. (3)) by minimizing the generalized χ^2. The advantage of this method is that it takes into account the fact that the different points of the correlation function are correlated. We define the generalized χ^2 as (Pollo et al. 2005),

$$\chi^2 = \sum_{i=1}^{N_\mathrm{p}}\sum_{j=1}^{N_\mathrm{p}}(w_\mathrm{p}^\mathrm{mod}(r_i) - w_\mathrm{p}^\mathrm{obs}(r_i))C_{ij}^{-1}(w_\mathrm{p}^\mathrm{mod}(r_j) - w_\mathrm{p}^\mathrm{obs}(r_j)) \quad (4)$$

where $w_\mathrm{p}^\mathrm{mod}(r_i)$ ($w_\mathrm{p}^\mathrm{obs}(r_i)$) is the value of $w_\mathrm{p}^\mathrm{mod}$ ($w_\mathrm{p}^\mathrm{obs}$) computed at $r_\mathrm{p} = r_i$ with $1 < i < N_\mathrm{p}$ (N_p is the number of r_p points), and C is the covariance matrix of the data estimated using bootstrap re-sampling. 100 bootstrap samples have been used in this analysis. The error bars estimated from the covariance matrix associated with the bootstrap samples only include the statistical error, and do not take into account errors due to cosmic variance. Therefore, in order to have a realistic estimation of the errors bars on our measurements, we compute $w_\mathrm{p}(r_\mathrm{p})$ on 50 mock VVDS surveys constructed using the *GalICS* simulation (Hatton et al. 2003). This simulation of hierarchical galaxy formation is based on a hybrid N-body/semi-analytic model, and is particularly well adapted to simulate the properties of the high-redshift galaxies that we observe in the VVDS (Blaizot et al. 2005; Pollo et al. 2005). Moreover, the selection function and the observational biases present in the VVDS dataset have been included in these mock samples (Pollo et al. 2005). Thus we fit the $w_\mathrm{p}(r_\mathrm{p})$ measurements from the simulations using the same method described previously, estimate the confidence limits on the r_0 and γ measurements using the $\Delta\chi^2$ distribution from the best fit (Pollo et al. 2005). The error bars obtained using this method are larger but more realistic than those from the bootstrap method. They include not only the statistical error but also the error from cosmic variance, which dominates in this case.

3.1.2. Computing the angular correlation function

In order to compute the angular two-point correlation function $w(\theta)$ (ACF), we use the Landy & Szalay estimator presented in Eq. (1), but in this case, simply considering angular pairs. Assuming that $w(\theta)$ is well described by a power-law model as $w(\theta) = A_w\theta^{1-\gamma}$, we fit the measured ACF to this model using the generalized χ^2 method and deduce the amplitude A_w and the slope $1-\gamma$. Because of the finite size of the survey, we introduce the integral constraint (IC) correction in our fitting procedure, defined as (Roche et al. 1993),

$$IC = \iint \frac{w(\theta)}{\Omega^2}\mathrm{d}\Omega_1\mathrm{d}\Omega_2 = \frac{A_w}{\Omega^2}\iint \theta^{1-\gamma}\mathrm{d}\Omega_1\mathrm{d}\Omega_2 = A_w B(\gamma) \quad (5)$$

with,

$$B(\gamma) = \frac{1}{\Omega^2}\iint \theta^{1-\gamma}\mathrm{d}\Omega_1\mathrm{d}\Omega_2 \quad (6)$$

where Ω is the area of the observed field. We compute $B(\gamma)$ by numerically integrating this expression over the entire data area, excluding regions where there are photometric defects. Our measurements are then fitted with the expression:

$$w_\mathrm{mod}(\theta) = A_w\theta^{1-\gamma} - IC = A_w(\theta^{1-\gamma} - B(\gamma)). \quad (7)$$

In order to derive the real-space correlation length r_0 from the angular correlation amplitude A_w, we use the Limber deprojection technique as described in Magliocchetti & Maddox (1999). This method, which is based on the Limber relativistic equation (Limber 1953), allows us to recover the value of r_0 if given A_w and the redshift distribution of the galaxies. In general, this technique is not stable, and the shape of the redshift distribution is critical. In this study however, we measure the ACF in relatively narrow redshift bins, so the shape we assume for the inversion is not critical. We use a smoothed redshift distribution by applying a moving window with a width of $\Delta z = 0.2$ to the initial photometric redshift distribution (Le Fèvre et al. 2007, in preparation). The width of the smoothing window has been chosen to reflect the typical uncertainty that we have on the photometric redshift values. The ACF error bars have been estimated using the bootstrap re-sampling method.

3.2. Clustering results

3.2.1. Clustering of the spectroscopic redshift sample

We compute $w_\mathrm{p}(r_\mathrm{p})$ in redshift intervals increasing from $z = 0.2$ to $z = 2.1$. We divide the 3.6 μm sub-sample in six redshift slices: [0.2, 0.5], [0.5, 0.7], [0.7, 0.9], [0.9, 1.1], [1.1, 1.3], [1.3, 2.1]. The 4.5 μm sub-sample has fewer objects than the 3.6 μm sample due to the slightly shallower depth. In order to maximize the number of objects per redshift slice, we consider in this case three slices only: [0.2, 0.7], [0.7, 1.1] and [1.1, 2.1].

In the fitting procedure, we use all the $w_\mathrm{p}(r_\mathrm{p})$ points for $0.1 \leq r_\mathrm{p} \leq 12\ h^{-1}$ Mpc. The projected correlation functions computed in each redshift slice are plotted in Fig. 4, along with the contours of confidence for the best-fitted parameters. Table 1 summarizes the values of the correlation length and the correlation function slope that we derive for the two sub-samples of the spectroscopic redshift sample.

The correlation length measured in the 3.6 μm and 4.5 μm sub-samples is roughly constant over the redshift range $z = [0.2,\ 2.1]$. It varies slightly between 3.8 and 4.2 h^{-1} Mpc, except in the high-redshift interval [1.3, 2.1] of the 3.6 μm sub-sample where a large correlation length of 5.8 h^{-1} Mpc is found. In this redshift range we are probing the intrinsically brightest galaxies, with a median absolute magnitude of $\langle M_B\rangle_\mathrm{Vega} = -22.13$ (Table 1). Compared to the characteristic absolute magnitude M_B^* at this redshift reported by Ilbert et al. (2005), it is found that for these objects, $\Delta M_B^* = \langle M_B\rangle - M_B^* \simeq -0.27$

Table 1. VVDS-SWIRE spectroscopic redshift sample: sub-sample properties and associated measurements of the slope, the correlation length, and the linear bias.

Spectroscopic redshift sample								
Sub-sample	Redshift interval	Mean redshift	Number of galaxies	$\langle M_B \rangle_{\rm Vega}$	γ	r_0 (h^{-1} Mpc)	r_0 (h^{-1} Mpc) (fixed $\gamma = 1.8$)	$b_{\rm L}$
3.6 μm	[0.2, 0.5]	0.36	336	−19.53	$1.92^{+0.27}_{-0.18}$	$3.8^{+0.6}_{-0.7}$	$3.9^{+0.6}_{-0.7}$	$0.93^{+0.10}_{-0.11}$
	[0.5, 0.7]	0.60	445	−20.29	$1.88^{+0.21}_{-0.14}$	$4.2^{+0.5}_{-0.5}$	$4.4^{+0.5}_{-0.5}$	$1.15^{+0.10}_{-0.10}$
	[0.7, 0.9]	0.81	512	−20.75	$1.77^{+0.15}_{-0.11}$	$3.8^{+0.4}_{-0.4}$	$3.7^{+0.4}_{-0.4}$	$1.15^{+0.09}_{-0.09}$
	[0.9, 1.1]	0.99	385	−21.17	$1.87^{+0.17}_{-0.14}$	$4.2^{+0.4}_{-0.4}$	$4.3^{+0.4}_{-0.4}$	$1.38^{+0.11}_{-0.11}$
	[1.1, 1.3]	1.19	195	−21.66	$2.44^{+0.22}_{-0.16}$	$3.8^{+0.5}_{-0.5}$	$3.7^{+0.5}_{-0.5}$	$1.62^{+0.43}_{-0.43}$
	[1.3, 2.1]	1.57	93	−22.13	$2.19^{+0.37}_{-0.38}$	$5.8^{+0.7}_{-1.0}$	$7.6^{+0.7}_{-1.0}$	$2.55^{+0.76}_{-0.96}$
4.5 μm	[0.2, 0.7]	0.48	485	−20.22	$1.84^{+0.18}_{-0.16}$	$3.9^{+0.5}_{-0.5}$	$3.9^{+0.5}_{-0.5}$	$1.01^{+0.08}_{-0.08}$
	[0.7, 1.1]	0.90	537	−21.15	$1.84^{+0.14}_{-0.14}$	$4.0^{+0.3}_{-0.4}$	$4.0^{+0.3}_{-0.4}$	$1.26^{+0.09}_{-0.10}$
	[1.1, 2.1]	1.42	182	−21.97	$1.82^{+0.26}_{-0.22}$	$3.7^{+0.6}_{-0.7}$	$3.7^{+0.6}_{-0.7}$	$1.48^{+0.24}_{-0.28}$

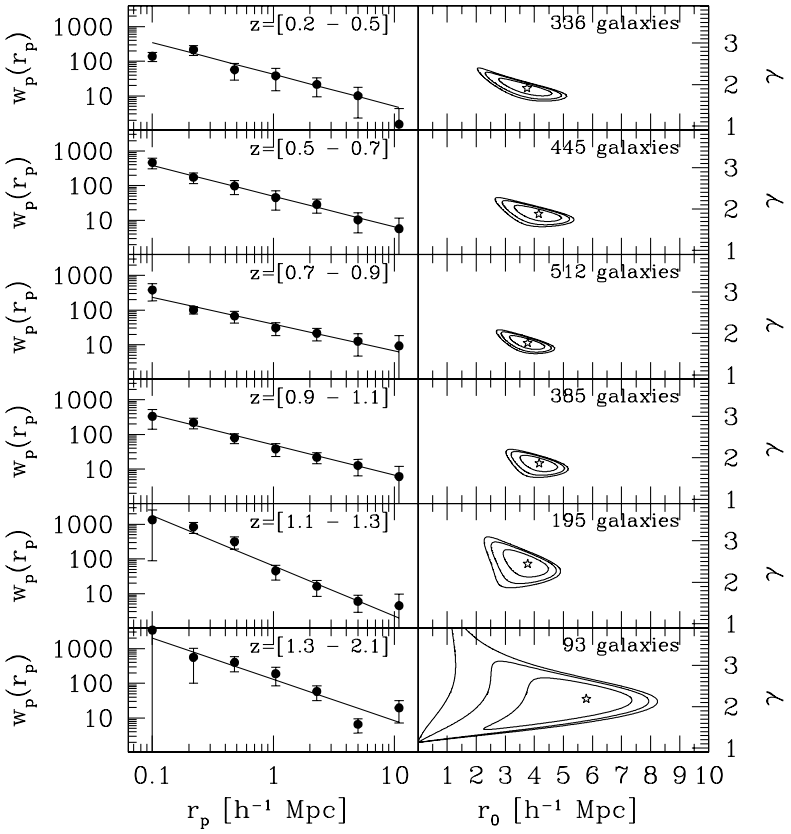

Fig. 4. *Left panels*: projected correlation functions for the 3.6 μm spectroscopic redshift sub-sample in different redshift slices with their best-fit power law. *Right panels*: the 68.3%, 90% and 95.4% confidence contours for the clustering parameters r_0 and γ.

and equivalently $\langle L_B \rangle / L_B^* \simeq 1.3$. Thus, these luminous galaxies are expected to be more strongly clustered as the halo clustering strength increases more rapidly for luminosities greater than a few times L^* (Zehavi et al. 2005; Norberg et al. 2002). Indeed Pollo et al. (2006); Coil et al. (2006) have shown that the galaxy correlation length increases more steeply for magnitude brighter than M^* at $z \simeq 1$, with r_0 values about 5 h^{-1} Mpc. Our high r_0 measurement in this high redshift bin is consistent with these findings. Moreover, in this redshift interval, the 1.6 μm rest-frame apparent emission feature from the photospheres of evolved stars (Simpson & Eisenhardt 1999) is present in the 3.6 μm band, favoring the detection of more massive and significantly more clustered systems (Farrah et al. 2006). We discuss in detail the evolution of the correlation length for the two sub-samples in Sect. 4.

3.2.2. Clustering of the photometric redshift sample

We measure the ACF and deduce the clustering parameters r_0 and γ for the photometric redshift sample in order to test the measurements from the spectroscopic redshift sample and to evaluate the effect of incompleteness.

Using the same methodology, we compute the ACF in increasing photometric redshift slices. We consider five slices: [0.2, 0.5], [0.5, 0.7], [0.7, 1.0], [1.0, 1.3] and [1.3, 1.7]. No redshift slices have been considered beyond $z_{\rm phot} = 1.7$ as the lack of accuracy of the photometric redshifts at these redshifts seriously corrupts the measurements.

We fit the measured ACF to a power-law model over $0.0017 \leq \theta \leq 0.1$ degrees. It is however evident, from Fig. 5, that the ACF departs from a power law model at scales greater

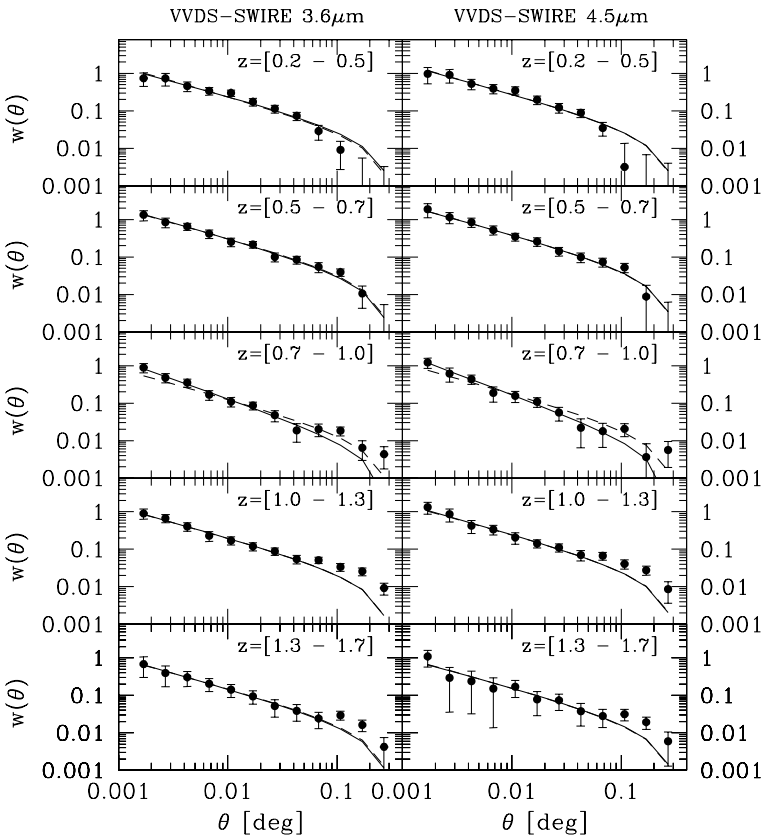

Fig. 5. The angular correlation function as a function of redshift, for the 3.6 μm and 4.5 μm photometric redshift sub-samples. The solid lines show the best-fit model when letting the two parameters free, while the dashed lines indicate the best-fit model with fixed $\gamma = 1.8$.

than ~0.1 degrees and at $z_{\rm phot} > 0.7$. This "excess" of power at large angular scales could be explained by the presence of another component in the correlation function, or by the presence of residual inhomogeneities in the field. We will explore this point in more detail in a future paper as it does not impact the results presented here.

The ACFs for the different redshift slices are plotted in Fig. 5. The best-fitted values of the angular correlation amplitude A_w, the correlation function slope γ and the correlation length r_0 that we derive with the Limber deprojection technique, are reported in Table 2.

Given the uncertainties on the ACF measurements, we adopt a fixed slope $\gamma = 1.8$. This is supported by the fact that, when letting both r_0 and γ vary in the ACF fitting, we find γ values very similar to 1.8, while the errors on r_0 increase slightly.

The values of the correlation length that we derive for the 3.6 μm and 4.5 μm photometric samples do not evolve with redshift up to $z_{\rm phot} = 1.7$. In the case of the 3.6 μm sub-sample, the r_0 values are in good agreement with the values found in the spectroscopic redshift sample. We observe slightly larger values of the correlation length for the 4.5 μm photometric redshift sub-sample than for the 4.5 μm spectroscopic redshift one. We interpret this as an effect of the incompleteness of the spectroscopic samples due to the I-band selection. To test this, we have measured in the photometric sample the clustering of the red population which is missed by the spectroscopic sample in the 3.6 μm and 4.5 μm bands. As most of the missed population is at redshifts $z_{\rm phot} > 1$, we have been able to perform this analysis only in the redshift range $z_{\rm phot} = [1, 1.7]$ where the available number of galaxies is large enough for a clustering signal to be measured. Results are presented in Fig. 3. We find that the clustering of the missed red population in the 3.6 μm spectroscopic sample has a correlation length of $r_0 = 5.6 \pm 1.0$, only marginally larger than that of the bulk of the population. Therefore, the clustering signal of the photometric and spectroscopic samples are very similar. For the red population in the 4.5 μm sample, we find that $r_0 = 8.8 \pm 2.4$, a significantly larger value that the main population. This explains why the spectroscopic sample slightly underestimates the clustering signal when compared to the photometric sample.

4. Discussion and conclusions

We first compare our measurements with previously reported results on samples of galaxies selected using Spitzer-IRAC bands. Oliver et al. (2004) use a similar galaxy selection; they define a flux-limited sample of SWIRE galaxies with $S_{3.6} > 32$ μJy, and they compute the ACF and deduce r_0 assuming a parametrized redshift distribution. The selection criterion they consider is different from the one we use, i.e. $S_{3.6} > 9.2$ μJy. This selects brighter galaxies than in our sample, that are expected to be more strongly clustered (Pollo et al. 2006; Coil et al. 2006). They find a correlation length $r_0 = 4.4 \pm 0.1$ h^{-1} Mpc at $z \simeq 0.75$ with $\gamma = 1.8$, which is higher than our value of $r_0 = 3.7 \pm 0.4$ h^{-1} Mpc at $z \simeq 0.81$. Taking into account that galaxies in their sample are 1.4 mag brighter and that brighter galaxies are on average more clustered, the two results are in good agreement.

We then compare our results with the clustering measurements of I-band selected VVDS-Deep galaxies (Le Fèvre et al. 2005a) in the same area. This comparison is shown in Fig. 6. We see that the correlation length is globally higher for near-infrared selected galaxies compared to optically-selected ones, and that

Table 2. VVDS-SWIRE photometric redshift sample: sub-sample properties and associated measurements of the ACF amplitude, the slope, and the correlation length.

Photometric redshift sample							
Sub-sample	Photometric redshift interval	Mean redshift	Number of galaxies	$A_w \times 10^3$	γ	r_0 (h^{-1} Mpc)	r_0 (h^{-1} Mpc) (fixed $\gamma = 1.8$)
3.6 μm	[0.2, 0.5]	0.37	2726	$7.7^{+4.7}_{-3.1}$	$1.76^{+0.10}_{-0.09}$	$4.2^{+1.5}_{-1.0}$	$4.0^{+0.3}_{-0.3}$
	[0.5, 0.7]	0.60	2714	$7.1^{+4.5}_{-3.0}$	$1.83^{+0.10}_{-0.09}$	$4.1^{+1.4}_{-0.9}$	$4.2^{+0.3}_{-0.3}$
	[0.7, 1.0]	0.85	5110	$1.2^{+0.8}_{-0.5}$	$2.03^{+0.11}_{-0.11}$	$2.8^{+1.0}_{-0.6}$	$3.4^{+0.2}_{-0.2}$
	[1.0, 1.3]	1.14	3577	$5.1^{+4.0}_{-2.5}$	$1.81^{+0.12}_{-0.11}$	$4.3^{+1.9}_{-1.1}$	$4.3^{+0.3}_{-0.3}$
	[1.3, 1.7]	1.47	2545	$3.4^{+3.7}_{-1.9}$	$1.83^{+0.16}_{-0.15}$	$4.0^{+2.4}_{-1.2}$	$4.1^{+0.4}_{-0.4}$
4.5 μm	[0.2, 0.5]	0.37	1977	$7.6^{+4.3}_{-2.8}$	$1.79^{+0.09}_{-0.10}$	$4.4^{+1.4}_{-0.9}$	$4.3^{+0.3}_{-0.3}$
	[0.5, 0.7]	0.60	1708	$10.4^{+8.5}_{-4.9}$	$1.80^{+0.13}_{-0.12}$	$4.8^{+2.2}_{-1.2}$	$4.8^{+0.3}_{-0.3}$
	[0.7, 1.0]	0.85	2971	$1.1^{+1.0}_{-0.5}$	$2.10^{+0.12}_{-0.13}$	$3.0^{+1.4}_{-0.7}$	$4.0^{+0.3}_{-0.3}$
	[1.0, 1.3]	1.14	2287	$6.1^{+7.1}_{-3.3}$	$1.81^{+0.15}_{-0.16}$	$4.8^{+3.1}_{-1.4}$	$4.8^{+0.4}_{-0.4}$
	[1.3, 1.7]	1.47	1700	$4.3^{+5.9}_{-2.5}$	$1.79^{+0.17}_{-0.19}$	$4.3^{+3.2}_{-1.4}$	$4.2^{+0.5}_{-0.5}$

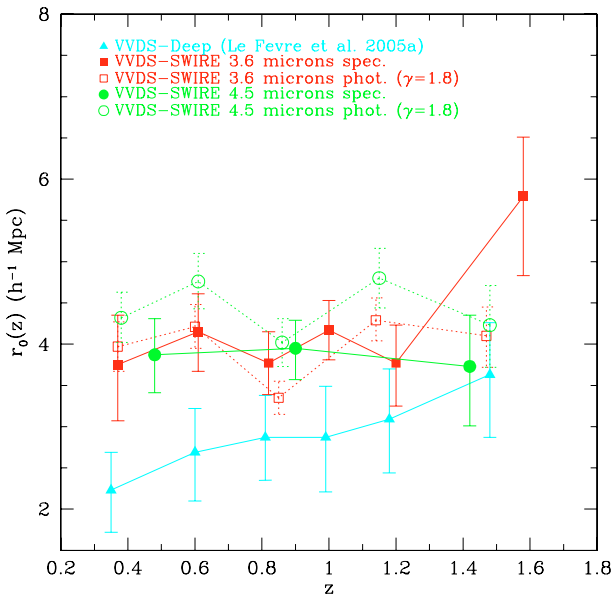

Fig. 6. Clustering evolution of VVDS-SWIRE samples of near-infrared galaxies compared to the VVDS-Deep I-band measurements. Filled symbols refer to measurements from spectroscopic samples while open symbols refer to measurements from photometric samples.

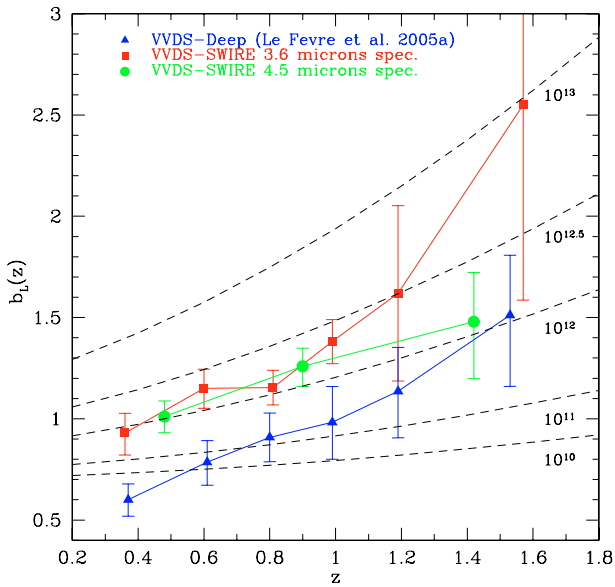

Fig. 7. Trend of the linear bias as a function of redshift for the VVDS-SWIRE 3.6 μm and 4.5 μm spectroscopic redshift samples compared to the VVDS-Deep I-band one. The dashed curves show the theoritical linear halo bias evolution for dark matter halos of mass greater than $10^{10}, 10^{11}, 10^{12}, 10^{12.5}$ and 10^{13} h^{-1} $M_\odot$ (from bottom to top). The linear galaxy bias is computed as described in Magliocchetti et al. (2000) from the r_0 and γ measurements. The theoretical curves have been computed using the fitting functions of Sheth & Tormen (1999) for the halo mass function and bias.

it is roughly constant over the redshift range $z = [0.2,\ 2.1]$. In comparison, r_0 from the I-selected sample shows a steady increase with redshift. As discussed in Sect. 3, the clustering of the 4.5 μm-selected galaxy population is higher as measured from the photometric sample than from the spectroscopic sample because the latter misses a significant fraction of red galaxies due to the additional $17.5 < I_{\rm AB} < 24$ cut applied by the VVDS-Deep survey selection. When comparing the measurements at 3.6 μm and 4.5 μm obtained from the photometric sample (open symbols in Fig. 6), we observe that the clustering of the sample selected at the reddest wavelength appears slightly stronger, although comparable within the errors. This is expected; selecting from longer wavelengths means we are sampling preferentially more early-types than later ones as described below. The color dependency of the clustering of galaxies in the VVDS-SWIRE sample will be reported elsewhere (de la Torre et al., in preparation).

In order to understand the systematically higher values of clustering that we find compared to those from optically-selected galaxies, and to quantify the type of galaxy population included in our near-infrared samples, we derive the spectral types of our spectroscopic redshift sample using the galaxy classification introduced by Zucca et al. (2006). This classification is based on the match to an empirical set of SEDs (as described in Arnouts et al. 1999) of the galaxy rest-frame colors. The redshift distributions per galaxy types are presented in Fig. 8 for the I-band, 3.6 μm and 4.5 μm selected samples. The four spectral types defined as type 1 to 4 correspond respectively to E/S0, early spiral, late spiral and irregular/starburst galaxies. One can see in Fig. 8 that the VVDS-Deep I-selected sample is dominated by late types (type 3 and 4) whereas the 4.5 μm selected sample is dominated by early types (type 1 and 2). In the 3.6 μm sample the different types balance out. Early type galaxies are known to be more clustered than late type ones at $z = 0$

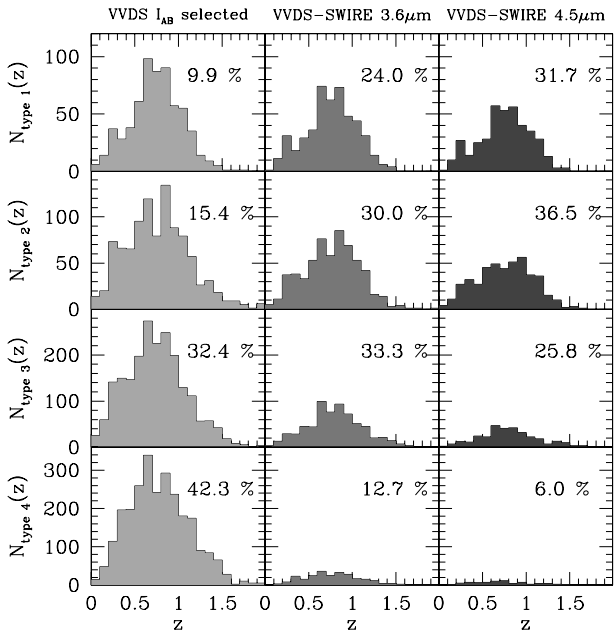

Fig. 8. Redshift distribution per spectral types for the 3.6 μm and 4.5 μm spectroscopic redshift sub-samples compared to the VVDS-Deep sample. We use the spectral types defined in Zucca et al. (2006): type 1 corresponds to E/S0, type 2 to early spiral, type 3 to late spiral and type 4 to irregular/starburst galaxies.

(e.g. Norberg et al. 2002; Zehavi et al. 2005) and also at high redshift (Meneux et al. 2006), thus the proportion of early type galaxies that we found in the different samples can explain why we measure higher values of clustering when galaxies are selected at longer wavelengths.

On the other hand, understanding the relatively constant clustering as a function of redshift that we observe in our near-infrared samples is not straightforward. Selecting galaxies at 3.6 μm or 4.5 μm, we are probing the rest-frame near-infrared emission, which is more sensitive to the emission from evolved stars. Therefore, our near-infrared selection should mostly be driven by stellar mass. As dark matter halo clustering is expected to decrease with increasing redshift (Weinberg et al. 2004), then under the reasonable assumption that stellar mass traces the underlying dark matter halo mass, one would expect the correlation length of our sample to decrease with increasing redshift. A contrary argument to this is that, as we select intrinsically more luminous galaxies with increasing redshift because of the magnitude selection of the sample, and since more luminous galaxies are more clustered (Pollo et al. 2006; Coil et al. 2006), we expect higher clustering strength as redshift increases. We suggest that these two competing arguments, working simultaneously, combine to produce the roughly constant clustering amplitude with redshift that we observe.

In order to check this hypothesis we examine the evolution of the linear galaxy bias for the different samples. We compute the galaxy linear bias $b_{\rm L}$ as described in Magliocchetti et al. (2000) from our r_0 and γ measurements. We define $b_{\rm L}$ as,

$$b_{\rm L}(z) = \frac{\sqrt{C_\gamma \left(r_0(z)/8\right)^\gamma}}{\sigma_{8,\rm mass}(z)},\ C_\gamma = \frac{72}{(3-\gamma)(4-\gamma)(6-\gamma)2^\gamma}. \quad (8)$$

This assumes a linear evolution of the rms mass fluctuations with cosmic time, i.e. $\sigma_{8,\rm mass}(z) = \sigma_{8,\rm mass}(z=0)D(z)$, $D(z)$ being the linear growth factor. We compare it to the theoretical halo bias evolution for dark matter halos of constant mass. To evaluate the linear halo bias we use the fitting functions of Sheth & Tormen (1999) for the halo mass function and bias. As shown in Fig. 7 the linear galaxy bias evolves more rapidly than the linear halo bias, indicating that these galaxies are not strictly mass-selected. Indeed because of our magnitude selection, we are probing more luminous, hence more biased galaxies at increasing redshifts. However, at least up to $z \simeq 1.5$ (and given the uncertainties), the linear galaxy bias for the rest-frame near-infrared galaxy samples seems to stay in between the linear halo bias tracks for halos of mass greater than 10^{12} and $10^{12.5}\ h^{-1}\ M_\odot$. This spread in mass is lower than the one for the rest-frame UV-optical VVDS-Deep sample, making this sample more suitable for tracing the passive growth of clustering with mass. This comparison of the linear galaxy bias and the linear halo bias is consistent with the idea that the clustering dependence on luminosity and stellar mass combine to produce a relatively constant clustering with redshift.

It is particularly interesting to note that at $z \simeq 1.5$, the correlation length of galaxies selected from the UV-optical rest-frame and hence actively star-forming is very similar to that of galaxies selected in the rest-frame near-infrared dominated by older stellar populations. This is quite different from what is observed in the local Universe, where selecting galaxies in the $K_{\rm s}$ band from 2MASS (Maller et al. 2005), it is found that these galaxies are significantly more clustered than those selected at optical wavelengths (SDSS EDR, Connolly et al. 2002). The galaxies which are making stars at $z \simeq 1.5$ therefore reside in similarly clustered regions as those containing the bulk of stellar mass, while at $z = 0$ the star formation happens in a population which is much less clustered than that where the bulk of stellar mass resides. This result is consistent with the observed flattening of the color-density relation above $z = 1.2-1.5$ (Cucciati et al. 2006), which indicates that, at these redshifts, blue star forming galaxies and red older galaxies are found to reside with equal probability in high or low density regions. Furthermore, we note that the clustering of massive luminous galaxies at $z \simeq 1.5$ is measured to be $r_0 \simeq 4\ h^{-1}$ Mpc, independently of the selection at optical or near-infrared wavelengths, while at lower redshifts the difference in the clustering strength measured from these samples increases. Galaxies selected via their UV-optical rest-frame show progressively lower clustering, whereas galaxies selected in the near-infrared (i.e. more mass-selected) stay comparably clustered. Taken together, this can be interpreted as evidence for star formation shifting from high density to low density regions, as cosmic time increases, another manifestation of the *downsizing* trend which has been indicated by observations over the last few years (e.g. Cowie et al. 1996). This underlines the primary role of mass in regulating star formation in galaxies (Gavazzi et al. 2002): while at high redshift star formation was strong in massive and more clustered galaxies, today it is mainly limited to lower mass, more uniformly distributed galaxies.

Acknowledgements. This research has been developed within the framework of the VVDS consortium.
This work has been partially supported by the CNRS-INSU and its Programme National de Cosmologie (France), and by Italian Ministry (MIUR) grants COFIN2000 (MM02037133) and COFIN2003 (Num. 2003020150).
The VLT-VIMOS observations have been carried out on guaranteed time (GTO) allocated by the European Southern Observatory (ESO) to the VIRMOS consortium, under a contractual agreement between the Centre National de la Recherche Scientifique of France, heading a consortium of French and Italian institutes, and ESO, to design, manufacture and test the VIMOS instrument.

References

Arnouts, S., Cristiani, S., Moscardini, L., et al. 1999, MNRAS, 310, 540
Bertin, E., & Arnouts, S. 1996, A&AS, 117, 393
Blaizot, J., Wadadekar, Y., Guiderdoni, B., et al. 2005, MNRAS, 360, 159

Bruzual, G., & Charlot, S. 2003, MNRAS, 344, 1000
Coil, A. L., Newman, J. A., Cooper, M. C., et al. 2006, ApJ, 644, 671
Connolly, A. J., Scranton, R., Johnston, D., et al. 2002, ApJ, 579, 42
Cowie, L. L., Songaila, A., Hu, E. M., & Cohen, J. G. 1996, AJ, 112, 839
Cucciati, O., Iovino, A., Marinoni, C., et al. 2006, A&A, 458, 39
Farrah, D., Lonsdale, C. J., Borys, C., et al. 2006, ApJ, 643, L139
Fisher, K. B., Davis, M., Strauss, M. A., Yahil, A., & Huchra, J. P. 1994, MNRAS, 267, 927
Gavazzi, G., Bonfanti, C., Sanvito, G., Boselli, A., & Scodeggio, M. 2002, ApJ, 576, 135
Hatton, S., Devriendt, J. E. G., Ninin, S., et al. 2003, MNRAS, 343, 75
Ilbert, O., Tresse, L., Zucca, E., et al. 2005, A&A, 439, 863
Ilbert, O., Arnouts, S., McCracken, H. J., et al. 2006, A&A, 457, 841
Iovino, A., McCracken, H. J., Garilli, B., et al. 2005, A&A, 442, 423
Kaiser, N. 1984, ApJ, 284, L9
Landy, S. D., & Szalay, A. S. 1993, ApJ, 412, 64
Le Fèvre, O., Vettolani, G., Paltani, S., et al. 2004, A&A, 428, 1043
Le Fèvre, O., Guzzo, L., Meneux, B., et al. 2005a, A&A, 439, 877
Le Fèvre, O., Vettolani, G., Garilli, B., et al. 2005b, A&A, 439, 845
Limber, D. N. 1953, ApJ, 117, 134
Lonsdale, C. J., Smith, H. E., Rowan-Robinson, M., et al. 2003, PASP, 115, 897
Magliocchetti, M., & Maddox, S. J. 1999, MNRAS, 306, 988
Magliocchetti, M., Bagla, J. S., Maddox, S. J., & Lahav, O. 2000, MNRAS, 314, 546
Maller, A. H., McIntosh, D. H., Katz, N., & Weinberg, M. D. 2005, ApJ, 619, 147
Meneux, B., Le Fèvre, O., Guzzo, L., et al. 2006, A&A, 452, 387
Norberg, P., Baugh, C. M., Hawkins, E., et al. 2002, MNRAS, 332, 827
Oliver, S., Waddington, I., Gonzalez-Solares, E., et al. 2004, ApJS, 154, 30
Pollo, A., Meneux, B., Guzzo, L., et al. 2005, A&A, 439, 887
Pollo, A., Guzzo, L., Le Fèvre, O., et al. 2006, A&A, 451, 409
Roche, N., Shanks, T., Metcalfe, N., & Fong, R. 1993, MNRAS, 263, 360
Rowan-Robinson, M., Babbedge, T., Surace, J., et al. 2005, AJ, 129, 1183
Sheth, R. K., & Tormen, G. 1999, MNRAS, 308, 119
Simpson, C., & Eisenhardt, P. 1999, PASP, 111, 691
Tajer, M., Polletta, M., Chiappetti, L., et al. 2007, A&A, 467, 73
Weinberg, D. H., Davé, R., Katz, N., & Hernquist, L. 2004, ApJ, 601, 1
White, S. D. M., & Rees, M. J. 1978, MNRAS, 183, 341
Zehavi, I., Zheng, Z., Weinberg, D. H., et al. 2005, ApJ, 630, 1
Zucca, E., Ilbert, O., Bardelli, S., et al. 2006, A&A, 455, 879

[1] Laboratoire d'Astrophysique de Marseille, UMR 6110 CNRS-Université de Provence, BP 8, 13376 Marseille Cedex 12, France
e-mail: sylvain.delatorre@oamp.fr
[2] INAF-Osservatorio Astronomico di Brera, via Brera 28, Milan, Italy
[3] Department of Astronomy, Cornell University, Space Sciences Building, Ithaca, NY 14853, USA
[4] Infrared Processing & Analysis Center, California Institute of Technology, MS 100-22, Pasadena, CA 91125, USA
[5] Center for Astrophysics & Space Sciences, University of California San Diego, La Jolla, CA 92093-0424, USA
[6] IASF-INAF, via Bassini 15, 20133 Milano, Italy
[7] Astronomy Centre, University of Sussex, Brighton BN1 9QH, UK
[8] INAF-Osservatorio Astronomico di Bologna, via Ranzani, 1, 40127 Bologna, Italy
[9] IRA-INAF, via Gobetti, 101, 40129 Bologna, Italy
[10] Spitzer Science Center, California Institute of Technology, Mail Stop 314-6, 1200 East California Boulevard, Pasadena, CA 91125, USA
[11] INAF-Osservatorio Astronomico di Capodimonte, via Moiariello 16, 80131 Napoli, Italy
[12] Università di Bologna, Dipartimento di Astronomia, via Ranzani 1, 40127 Bologna, Italy
[13] Laboratoire d'Astrophysique de l'Observatoire Midi-Pyrénées (UMR 5572), 14 avenue E. Belin, 31400 Toulouse, France
[14] Max Planck Institut fur Astrophysik, 85741, Garching, Germany
[15] Institut d'Astrophysique de Paris, UMR 7095, 98bis Bvd. Arago, 75014 Paris, France
[16] Observatoire de Paris, LERMA, 61 avenue de l'Observatoire, 75014 Paris, France
[17] Astrophysical Institute Potsdam, An der Sternwarte 16, 14482 Potsdam, Germany
[18] INAF-Osservatorio Astronomico di Roma, via di Frascati 33, 00040 Monte Porzio Catone, Italy
[19] Universitá di Milano-Bicocca, Dipartimento di Fisica, Piazza delle Scienze 3, 20126 Milano, Italy
[20] Integral Science Data Centre, Ch. d'Écogia 16, 1290 Versoix, Switzerland
[21] Geneva Observatory, ch. des Maillettes 51, 1290 Sauverny, Switzerland
[22] Astronomical Observatory of the Jagiellonian University, ul Orla 171, 30-244 Kraków, Poland
[23] Centre de Physique Théorique, UMR 6207 CNRS-Université de Provence, 13288 Marseille, France
[24] Centro de AstrofÃŋsica da Universidade do Porto, Rua das Estrelas, 4150-762 Porto, Portugal
[25] Institute for Astronomy, 2680 Woodlawn Dr., University of Hawaii, Honolulu, 96822, Hawaii
[26] School of Physics & Astronomy, University of Nottingham, University Park, Nottingham, NG72RD, UK